The Astronomical Journal, 162:135 (13pp), 2021 October https://doi.org/10.3847/1538-3881/ac1940

TOI-532b: The Habitable-zone Planet Finder confirms a Large Super Neptune in the Neptune Desert orbiting a metal-rich M-dwarf host

Shubham Kanodia[1,2], Gudmundur Stefansson[3,26], Caleb I. Cañas[1,2,27], Marissa Maney[1,2], Andrea S. J. Lin[1,2], Joe P. Ninan[1,2], Sinclaire Jones[3], Andrew Monson[1,2], Brock A. Parker[4], Henry A. Kobulnicky[4], Jason Rothenberg[4], Corey Beard[5], Jack Lubin[6], Paul Robertson[6], Arvind F. Gupta[1,2], Suvrath Mahadevan[1,2], William D. Cochran[7,8], Chad F. Bender[9], Scott A. Diddams[10,11], Connor Fredrick[10,11], Samuel Halverson[12], Suzanne Hawley[13], Fred Hearty[1,2], Leslie Hebb[14], Ravi Kopparapu[15,16], Andrew J. Metcalf[17,18,19], Lawrence W. Ramsey[1,2], Arpita Roy[20,21], Christian Schwab[22], Maria Schutte[23], Ryan C. Terrien[24], John Wisniewski[23], and Jason T. Wright[1,2,25]

[1] Department of Astronomy & Astrophysics, 525 Davey Laboratory, The Pennsylvania State University, University Park, PA 16802, USA; shbhuk@gmail.com
[2] Center for Exoplanets and Habitable Worlds, 525 Davey Laboratory, The Pennsylvania State University, University Park, PA 16802, USA
[3] Department of Astrophysical Sciences, Princeton University, 4 Ivy Lane, Princeton, NJ 08540, USA
[4] Department of Physics & Astronomy, University of Wyoming, Laramie, WY 82070, USA
[5] Department of Physics and Astronomy, The University of California, Irvine, Irvine, CA 92697, USA
[6] Department of Physics & Astronomy, University of California Irvine, Irvine, CA 92697, USA
[7] McDonald Observatory and Department of Astronomy, The University of Texas at Austin, USA
[8] Center for Planetary Systems Habitability, The University of Texas at Austin, USA
[9] Steward Observatory, The University of Arizona, 933 N. Cherry Avenue, Tucson, AZ 85721, USA
[10] Time and Frequency Division, National Institute of Standards and Technology, 325 Broadway, Boulder, CO 80305, USA
[11] Department of Physics, University of Colorado, 2000 Colorado Avenue, Boulder, CO 80309, USA
[12] Jet Propulsion Laboratory, 4800 Oak Grove Drive, Pasadena, CA 91109, USA
[13] Department of Astronomy, Box 351580, University of Washington, Seattle, WA 98195 USA
[14] Department of Physics, Hobart and William Smith Colleges, 300 Pulteney Street, Geneva, NY 14456, USA
[15] NASA Goddard Space Flight Center, 8800 Greenbelt Road, Greenbelt, MD 20771, USA
[16] Sellers Exoplanet Environment Collaboration (SEEC), NASA Goddard Space Flight Center USA
[17] Space Vehicles Directorate, Air Force Research Laboratory, 3550 Aberdeen Avenue SE, Kirtland AFB, NM 87117, USA
[18] Time and Frequency Division, National Institute of Technology, 325 Broadway, Boulder, CO 80305, USA
[19] Department of Physics, 390 UCB, University of Colorado Boulder, Boulder, CO 80309, USA
[20] Space Telescope Science Institute, 3700 San Martin Drive, Baltimore, MD 21218, USA
[21] Department of Physics and Astronomy, Johns Hopkins University, 3400 N Charles Street, Baltimore, MD 21218, USA
[22] Department of Physics and Astronomy, Macquarie University, Balaclava Road, North Ryde, NSW 2109, Australia
[23] Homer L. Dodge Department of Physics and Astronomy, University of Oklahoma, 440 W. Brooks Street, Norman, OK 73019, USA
[24] Department of Physics and Astronomy, Carleton College, One North College Street, Northfield, MN 55057, USA
[25] Penn State Extraterrestrial Intelligence Center, 525 Davey Laboratory, The Pennsylvania State University, University Park, PA, 16802, USA
Received 2021 June 16; accepted 2021 July 28; published 2021 September 9

Abstract

We confirm the planetary nature of TOI-532b, using a combination of precise near-infrared radial velocities with the Habitable-zone Planet Finder, Transiting Exoplanet Survey Satellite (TESS) light curves, ground-based photometric follow up, and high-contrast imaging. TOI-532 is a faint ($J \sim 11.5$) metal-rich M dwarf with $T_{\rm eff} = 3957 \pm 69$ K and $[{\rm Fe/H}] = 0.38 \pm 0.04$; it hosts a transiting gaseous planet with a period of ~2.3 days. Joint fitting of the radial velocities with the TESS and ground-based transits reveal a planet with radius of 5.82 ± 0.19 $R_\oplus$, and a mass of $61.5^{+9.7}_{-9.3}$ $M_\oplus$. TOI-532b is the largest and most massive super Neptune detected around an M dwarf with both mass and radius measurements, and it bridges the gap between the Neptune-sized planets and the heavier Jovian planets known to orbit M dwarfs. It also follows the previously noted trend between gas giants and host-star metallicity for M-dwarf planets. In addition, it is situated at the edge of the Neptune desert in the Radius–Insolation plane, helping place constraints on the mechanisms responsible for sculpting this region of planetary parameter space.

Unified Astronomy Thesaurus concepts: Extrasolar gaseous planets (2172); Radial velocity (1332); Transit photometry (1709); Hot Neptunes (754)

1. Introduction

Studies analyzing the host-star metallicity dependence of gas giant ($R > 4$ $R_\oplus$) occurrence rates have traditionally relied on a sample of planets orbiting solar type stars, with a typical minimum photospheric temperature corresponding to mid-K dwarfs. Extending this analysis to M-dwarf planets has been hampered by the intrinsic faintness of M dwarfs, which makes planet detection and mass measurement difficult. Occurrence rate studies for transiting planets orbiting M dwarfs have been limited to the smaller ($R < 4$ $R_\oplus$) planets (Laughlin et al. 2004; Johnson & Apps 2009; Gaidos et al. 2013; Dressing & Charbonneau 2015; Hsu et al. 2020). Attempts to study the occurrence rates of gas giants orbiting M dwarfs have used samples from radial-velocity (RV) surveys (Johnson & Apps 2009; Johnson et al. 2010; Gaidos et al. 2013; Tuomi et al. 2019). Most recently, Maldonado et al. (2020) use a sample of RV planets detected from the HARPS-N spectrograph to probe the dependence of gas giant occurrence on

[26] Henry Norris Russell Fellow.
[27] NASA Earth and Space Science Fellow.

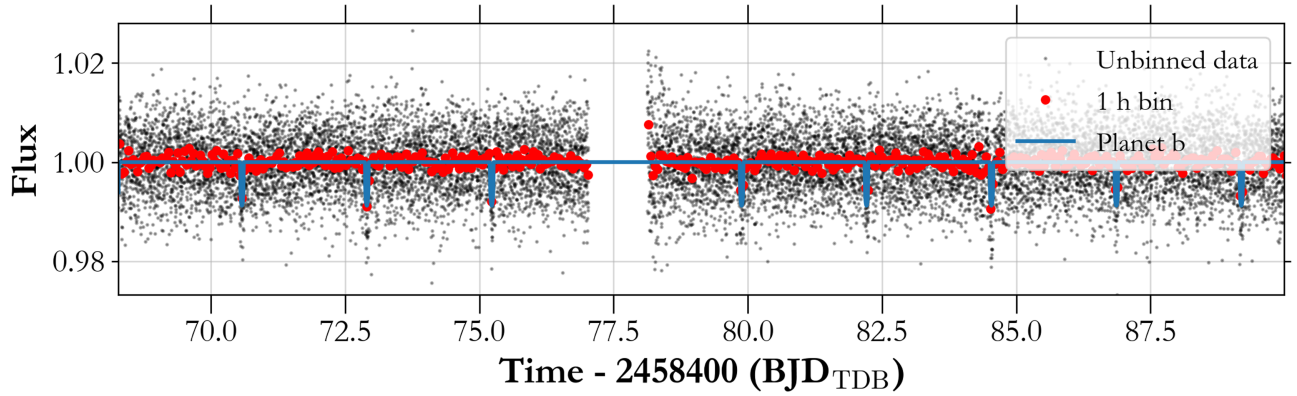

Figure 1. Short cadence (2 minute) time series TESS PDCSAP photometry (without detrending) from Sector 6, with the binned data (in 1 hr bins), along with the TOI-532b transits overlaid in blue.

metallicity. Occurrence rate studies for gaseous planets using RV surveys can be complicated by the lack of true mass measurements (M_p versus M_p sin$i$). Therefore, in its all-sky survey of transiting planets around nearby stars—and with its red-optimized bandpass yielding high precision photometric observations of nearby M dwarfs— the Transiting Exoplanet Survey Satellite (TESS; Ricker et al. 2014) presents a unique opportunity to find transiting gas giants orbiting M dwarfs suitable for mass measurements. Four such recent discoveries by TESS are TOI-1728b (Kanodia et al. 2020), TOI-1899b (Cañas et al. 2020), TOI-442b (Dreizler et al. 2020), and TOI-674b (Murgas et al. 2021).

Transiting Neptune-sized planets ($2R_\oplus < R_p < 6R_\oplus$),[28] present a transitional population between rocky terrestrial planets and Jovian gas giants. In particular, transiting super Neptunes ($17M_\oplus < M_p < 57M_\oplus$; Bakos et al. 2015) can help inform theories of planet formation and migration, i.e., did the gaseous giants form in situ close to their host star or form away beyond the ice line and migrate inwards due to eccentricity driven excitation or disk migration (Madhusudhan et al. 2017; Bean et al. 2020; Fortney et al. 2021). This investigation into the provenance of gaseous giants can be further aided by atmospheric characterization using transmission spectroscopy (Guzmán-Mesa et al. 2020), where the "warm Neptunes" with equilibrium temperatures between ~800–1200 K, are expected to exhibit diverse atmospheric elemental abundances, with possible imprints of the protoplanetary disk chemistry (Mordasini et al. 2016).

Additionally, as predicted by Ida & Lin (2004a), Szabó & Kiss (2011), and Mazeh et al. (2016) have noted a dearth of Neptune-sized objects orbiting close to their host star (2–4 day orbital period), referred to as the "Neptune Desert." Different hypotheses have been proposed as a possible explanation to this feature, since it can not be explained by observational biases. Matsakos & Königl (2016) attempt to explain the origin of the Neptune Desert using high-eccentricity migration, whereas Owen & Lai (2018) show that photoevaporation can be a driving factor responsible for the lower boundary of the desert.

In this manuscript, we report the discovery of the transiting super Neptune TOI-532b using precision RVs from the near-infrared (NIR) Habitable-zone Planet Finder (HPF; Mahadevan et al. 2012, 2014) spectrograph, to measure the mass of a transiting super Neptune orbiting the early type metal-rich M-dwarf TOI-532 in the constellation of Orion. We perform a comprehensive characterization of the stellar and planetary properties using space-based photometric observations from TESS, additional ground-based transit observations, adaptive optics imaging, and high-contrast speckle imaging. This paper is structured as follows. In Section 2, we discuss the observations of this system, which include space-based TESS photometry, ground-based photometry, high-contrast imaging, as well as precision RV observations with HPF. In Section 3 we discuss our characterization of the stellar parameters, followed by Section 4, where we detail our joint analysis of the photometry and velocimetry to constrain the planetary parameters of TOI-532b. In Section 5, we compare the properties of TOI-532b with other M-dwarf exoplanets, and with few other Neptunes to place it in context for potential He 10830 Å absorption detection using transmission spectroscopy. Finally, we summarize our results in Section 6.

2. Observations

2.1. TESS

TOI-532 (TIC-144700903, 2MASS J05401918+1133463, Gaia EDR3 3340265717587057536, UCAC4 508-014156) was observed by TESS in Sector 6 in Camera 1 from 2018 December 11 to 2019 January 7th at a 2 minute cadence (Figure 1). The Science Processing Operations Center (SPOC) at NASA Ames (Jenkins et al. 2016) reported one transiting planet candidate, TOI-532.01, with a period of 2.326811 days. For our subsequent analysis, we use the Presearch Data Conditioning Single Aperture Photometry (PDCSAP) light curve, which contains systematics and dilution corrected data using the algorithms originally developed for the Kepler data analysis pipeline. We retrieved the data using the `lightkurve` package (Lightkurve Collaboration et al. 2018), available at the Mikulski Archive for Space Telescopes (MAST).

Figure 2 presents a comparison of the region contained within the Sector 6 footprint from the Palomar Observatory Sky Survey (POSS-1; Harrington 1952; Minkowski & Abell 1963) image in 1951 and a more recent ZTF (Masci et al. 2019) image from 2019. There are no bright targets with Δ $G_{RP} < 3$ present in the TESS aperture; however, there are a few targets with Δ $G_{RP} < 4$ that dilute the TESS transit. Even though this is taken into account in the PDCSAP flux, following the methodology of Burt et al. (2020) we use our ground-based photometry to estimate an additional correction to this dilution term photometry and discuss this in Section 4.

[28] Also referred to as sub-Saturns (Kopparapu et al. 2018; Petigura et al. 2018).

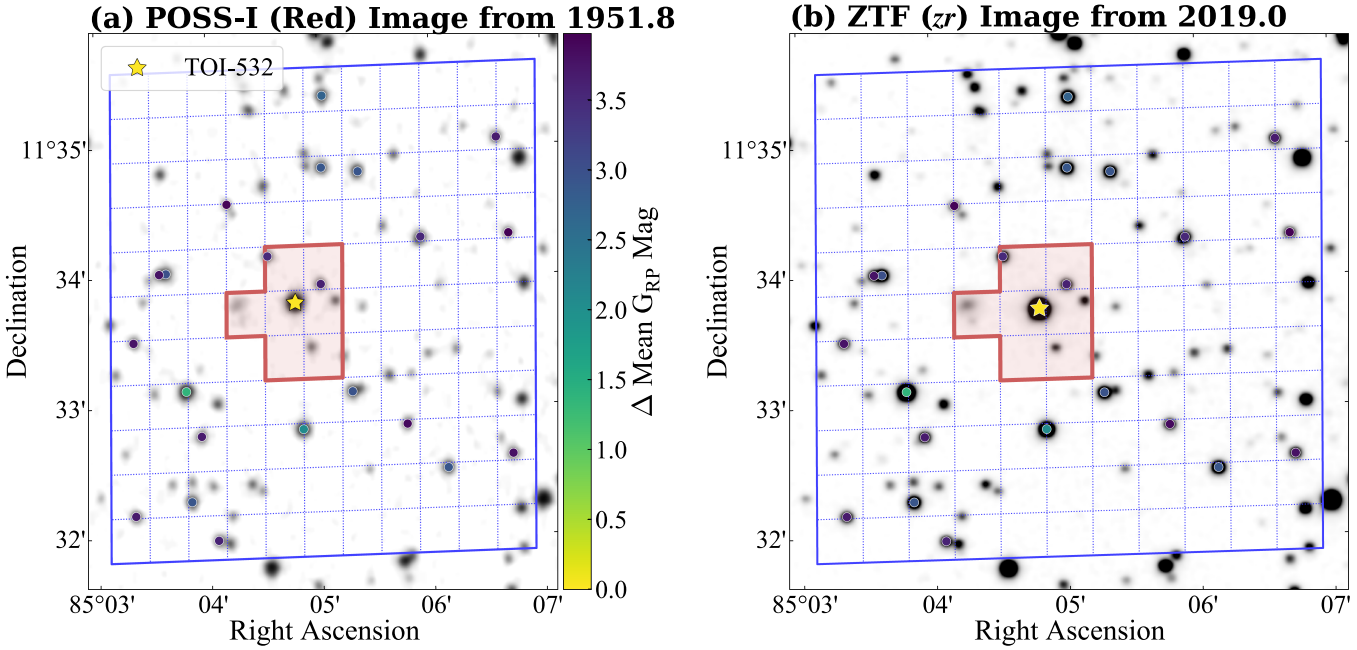

Figure 2. Panel (a) overlays the 11 × 11 pixel TESS Sector 6 footprint (blue grid) on a POSS-I red image from 1951.8. TOI-532 does not have significant proper motion, as can be seen while comparing panel (a) and (b). The TESS aperture is outlined in red and we highlight our target TOI-532. No bright targets are present inside the TESS aperture with Δ G_{RP} < 3. Panel (b) is similar to panel (a) but with a background image from ZTF *zr* (5600–7316 Å) 2019 (Masci et al. 2019).

2.2. Ground-based Photometric Follow Up

We obtain follow-up transits from the ground, to validate the transit seen in the TESS photometry, and measure the dilution present therein. Furthermore, the ground-based photometry helps in improving the radius estimates as well as the ephemeris. These observations were pipeline processed using standard linearity, bias, dark, and flat-field corrections. We then performed aperture photometry using AstroImageJ (Collins et al. 2017). Clear outliers due to cosmic rays, charged-particle events, poor seeing conditions, or telescope tracking were removed using AstroImageJ. We experimented using a number of different aperture settings, and varied the radii of the photometric aperture, as well as the inner, and outer background annuli, and selected the settings that resulted in the minimum scatter in the resulting photometry. Following the methodology in Stefansson et al. (2017), we added the scintillation error estimates to the photometric error estimated by AstroImageJ. See Figure 3 and Table 1 for a summary of all our ground-based photometric observations.

2.2.1. RBO

We observed a transit of TOI-532b on the night of 2020 December 7 using the 0.6 m telescope at the Red Buttes Observatory (RBO) in Wyoming (Kasper et al. 2016). The RBO telescope is a f/8.43 Ritchey–Chrétien Cassegrain constructed by DFM Engineering, Inc. It is currently equipped with an Apogee ASPEN CG47 camera.

The target rose from an air mass of 1.61 at the start of the observations to a minimum air mass of 1.15 and then set to an air mass of 1.20 at the end of the observations. Observations were performed using the Bessell I filter (Bessell 1990) with 1 × 1 on-chip binning. To prevent saturation, we defocused moderately (Table 1), which allowed us to use an exposure time of 120 s. In the 1 × 1 binning mode, the 0.6 m at RBO has a gain of 1.27 e/ADU, a plate scale of 0.″532, and a readout time of approximately 2.4 s.

Due to cloud contamination, only the transit ingress was recovered from these observations (Figure 3(b)). For the final reduction, we selected a photometric aperture of 17 pixels (9.″04) with an inner sky annulus of 40 pixels (21.″3) and outer sky annulus of 60 pixels (31.″9).

2.2.2. Three-hundred MilliMeter (300mm) Telescope

We observed two transits of TOI-532b on the nights of 2020 December 15 (Figure 3(c)) and 2021 January 4 (Figure 3(e)) using the Three-hundred MilliMeter (300 mm) Telescope (TMMT; Monson et al. 2017) at Las Campanas Observatory in Chile. TMMT is a f/7.8 FRC300 from Takahashi on a German equatorial AP1600 GTO mount with an Apogee Alta U42-D09 CCD Camera, FLI ATLAS focuser, and Centerline filter wheel.

On 2020 December 15, the target rose from an air mass of 1.86 at the start of the observations to a minimum air mass of 1.32 and then set to an air mass of 2.62 at the end of the observations. On 2021 January 4, the target rose from an air mass of 1.48 to a minimum air mass of 1.32 and then set to an air mass of 3.16 at the end of observations. Observations on both nights were performed using the Bessell I filter with 1 × 1 on-chip binning and exposure times of 120 s. In the 1 × 1 binning mode, TMMT has a gain of 1.35 e/ADU, a plate scale of 1.″194 pixel^{-1}, and a readout time of 6 s.

In addition to the standard corrections, a fringe subtraction was also performed for the TMMT I band images. The final light curve from 2020 December 15 utilized a photometric aperture of 5 pixels (5.″97), an inner sky annulus of 20 pixels (23.″9), and a outer sky annulus of 30 pixels (35.″8). The final light curve from 2021 January 4 utilized a photometric aperture of 5 pixels (5.″97), an inner sky annulus of 15 pixels (17.″9) and outer sky annulus of 30 pixels (35.″8).

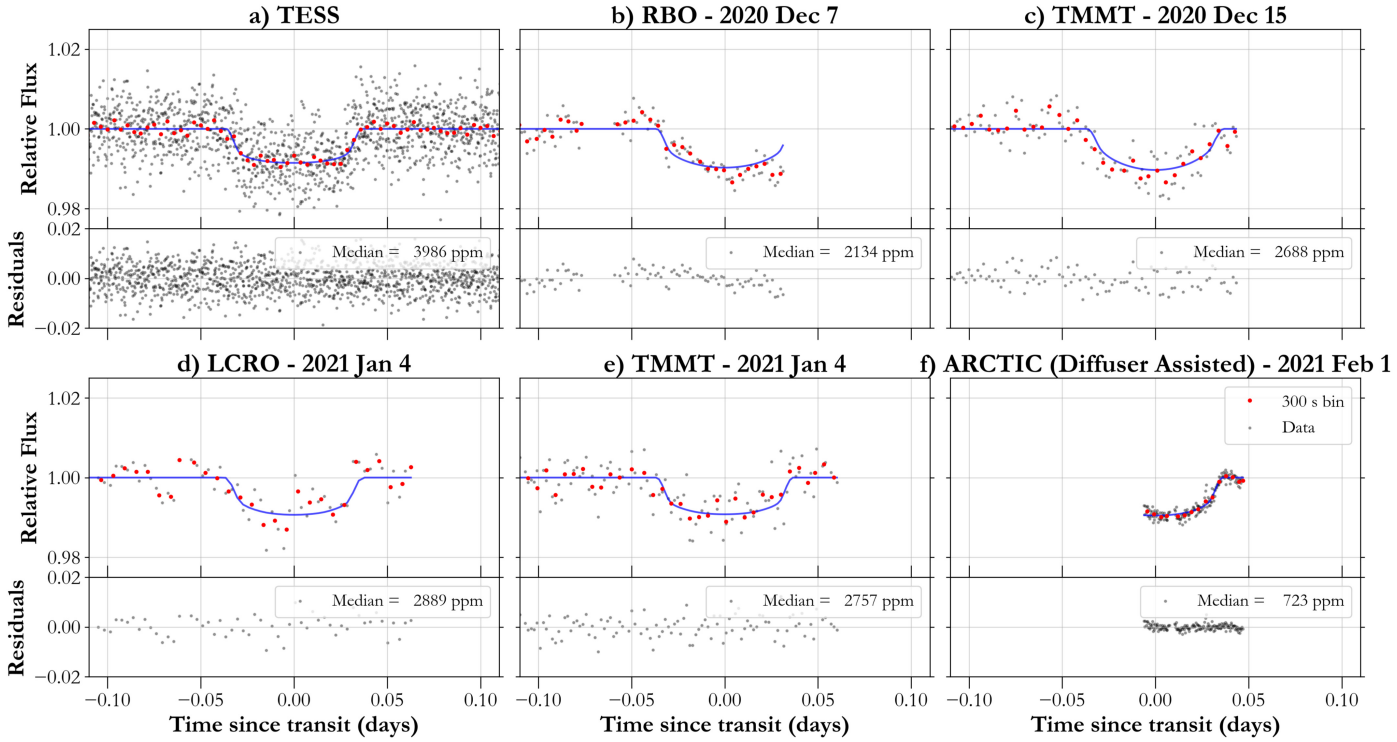

Figure 3. Photometric observations for TOI-532b: (a) the TESS phased plot shows the light curve phase folded to the best-fit orbital period; (b–f) ground-based observations for TOI-532b. The raw photometery is shown in gray, whereas in red we show the photometry binned to 5 minute bins. The best-fit transit solution, along with the 1 σ confidence interval, are shown in blue.

Table 1
Summary of Ground-based Photometric Follow Up of TOI-532

Obs Date (YYYY-MM-DD)	Filter	Exposure Time (s)	PSF FWHM ($''$)	Apertures: Photometric, Inner, Outer Annuli ($''$)	Field of View (prime)
			RBO (0.6 m)		
2020-12-07	Bessell I	120	8.88 (Defocus)	9.04, 21.3, 31.9	8.94 × 8.94
			TMMT (0.3 m)		
2020-12-15	Bessell I	120	3.49	5.97, 23.9, 35.8	40.75 × 40.75
2021-01-04	Bessell I	120	3.18	5.97, 17.9, 35.8	40.75 × 40.75
			LCRO (0.3 m)		
2021-01-04	i'	240	2.45	4.64, 10.0, 23.2	51.97 × 51.97
			APO (3.5 m)		
2021-02-01	i'	20	7.67 (Diffuser[a])	5.72, 13.2, 19.8	7.9 × 7.9

Note.
[a] Engineered diffuser with $8\farcs7$ FWHM (Stefansson et al. 2017).

2.2.3. LCRO

We observed a transit of TOI-532b on the night of 2021 January 4 (Figure 3(d)) using the 305 mm Las Campanas Remote Observatory (LCRO) telescope at the Las Campanas Observatory in Chile. The LCRO telescope is an f/8 Maksutov–Cassegrain from Astrophysics on a German Equatorial AP1600 GTO mount with an FLI Proline 16803 CCD Camera, FLI ATLAS focuser, and Centerline filter wheel.

The target rose from an air mass of 1.40 at the start of the observations to a minimum air mass of 1.32 and then set to an air mass of 3.29 at the end of the observations. Observations were performed using the SDSS i' filter with 1×1 on-chip binning and an exposure time of 240 s. In the 1×1 binning mode, LCRO has a gain of 1.52 e/ADU, and a plate scale of $0\farcs773\,\mathrm{pixel}^{-1}$, and a readout time of 17 s. For the final reduction, we selected a photometric aperture of 6 pixels ($4\farcs64$) with an inner sky annulus of 13 pixels ($10\farcs0$) and outer sky annulus of 30 pixels ($23\farcs2$).

2.2.4. Diffuser-assisted Photometry with the 3.5 m ARC Telescope

We observed a transit of TOI-532b (Figure 3(f)) on the night of 2021 February 1 using the 3.5 m Astrophysical Research Consortium (ARC) Telescope Imaging Camera (ARCTIC; Huehnerhoff et al. 2016) at the ARC 3.5 m Telescope at Apache Point Observatory (APO). We observed the transit using the Engineered Diffuser available on ARCTIC, which we designed to enable precision photometric observations from the ground on nearby bright stars (Stefansson et al. 2017).

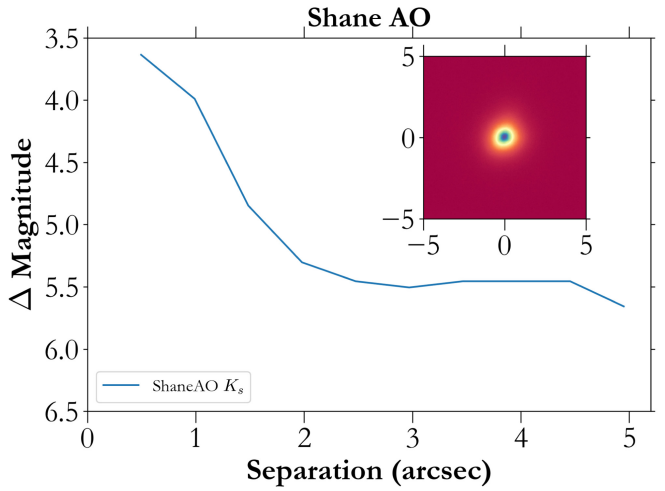

Figure 4. 5σ contrast curve for TOI-532 from the ShARCS camera on the Shane 3 m telescope. We detected no companions within $0\farcs507 \pm 0\farcs017$ corresponding to a ΔKs of 3.7. The inset shows a $10''$ region around the star.

The target set from an air mass of 1.07 at the start of the observations to an air mass of 1.14 at the end of the observations. The observations were performed using the SDSS i' filter with an exposure time of 20 s in the LL-readout and fast-readout modes with 4×4 on-chip binning. In the 4×4 binning mode, ARCTIC has a gain of 2.0 e/ADU, a plate scale of $0\farcs456$ pixel^{-1}, and a readout time of 2.7 s. Due to cloud contamination, only the egress of the transit was recovered from the data. For the final reduction, we selected a photometric aperture of 13 pixels ($5\farcs72$), an inner sky annulus of 30 pixels ($13\farcs2$), and outer sky annulus of 45 pixels ($19\farcs8$).

2.3. High-contrast Imaging

2.3.1. ShARCS on the Shane Telescope

We observed TOI-532 using the ShARCS camera on the Shane 3 m telescope at Lick Observatory (Srinath et al. 2014). Due to instrument repairs, we were unable to use the Laser Guide Star mode, and had to use Natural Guide Star mode. This mode can be more challenging for faint targets, as the guider camera can easily lose the target, but conditions were good enough to retrieve data for TOI-532. The target was observed using a five-point dither process as outlined in Furlan et al. (2017).

The data is then reduced using a custom AO pipeline developed internally. This pipeline first rejects all overexposed or underexposed images, and we then manually exclude data we know to be erroneous (lost guiding on the star, shutters closed early due to weather, etc). Next we apply a standard dark correction, flat correction, and sigma clipping process. A master sky image is produced from the 5 point dither process, and subtracted from each image. A final image is then produced using an interpolation process to shift the images onto a single centroid.

Finally, we use the algorithm developed by Espinoza et al. (2016) to generate a 5 sigma contrast curve as a part of the final analysis (Figure 4). We detected no companions within $>0\farcs507$ corresponding to a ΔKs of 3.7.

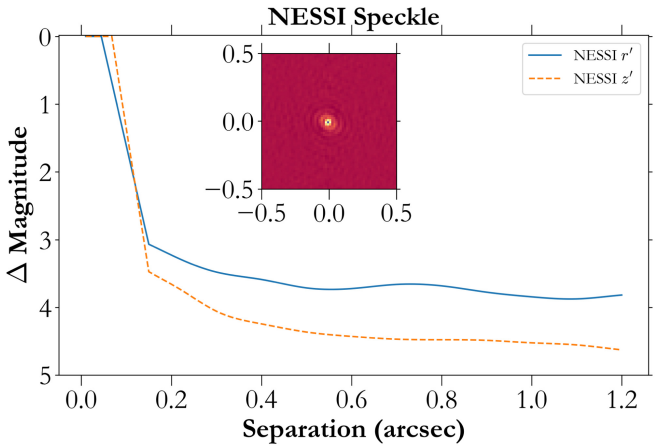

Figure 5. 5σ contrast curve for TOI-532 observed from NESSI in the Sloan r' and z' filters showing no bright companions within $1\farcs2$ from the host star. The z' image is shown as an inset $1''$ across.

2.3.2. NN-Explore Exoplanet Stellar Speckle Imager at WIYN

We supplement our AO data with speckle imaging observations taken on 2021 April 3 using the NN-Explore Exoplanet Stellar Speckle Imager (NESSI) on the WIYN 3.5 m telescope at Kitt Peak National Observatory. To search for faint background stars and stellar companions, we collected a 9 minute sequence of 40 ms diffraction-limited exposures of TOI-532 with the Sloan r' and z' filters. As we show in Figure 5, the NESSI data show no evidence of blending from a bright companion at separations $>0\farcs15$ at $\Delta r' = 3.1$, and $\Delta z' = 3.5$.

2.4. Radial-velocity Follow Up with the Habitable-zone Planet Finder

We observed TOI-532 using HPF (Mahadevan et al. 2012, 2014), a NIR (8080–12780 Å), high-resolution precision RV spectrograph located at the 10 meter Hobby–Eberly Telescope (HET) in Texas. HET is a fixed-altitude telescope with a roving pupil design. It is fully queue-scheduled telescope with all observations executed in a queue by the HET resident astronomers (Shetrone et al. 2007). HPF is a fiber-fed instrument with a separate science, sky, and simultaneous calibration fiber (Kanodia et al. 2018), and is actively temperature stabilized at the milli-Kelvin level (Stefansson et al. 2016). We use the algorithms described in the tool `HxRGproc` for bias removal, nonlinearity correction, cosmic-ray correction, slope/flux, and variance image calculation (Ninan et al. 2018) of the raw HPF data. HPF has the capability for simultaneous calibration using a NIR Laser Frequency Comb (LFC; Metcalf et al. 2019); however owing to the faintness of our target we chose to avoid simultaneous calibration to minimize the impact of scattered calibrator light in the science target spectra. Instead, we interpolate the wavelength solution from other LFC exposures on the night of the observations, to correct for the well calibrated instrument drift, as has been discussed in Stefansson et al. (2020). This method has been shown to enable precise wavelength calibration and drift correction with a precision of $\sim$30 cm s^{-1} per observation, a value much smaller than our estimated per observation RV uncertainty (instrumental + photon noise) for this object of $\sim$22 m s^{-1} (in 649 s exposures).

To estimate the RVs, we follow the method described in Stefansson et al. (2020), by using a modified version of

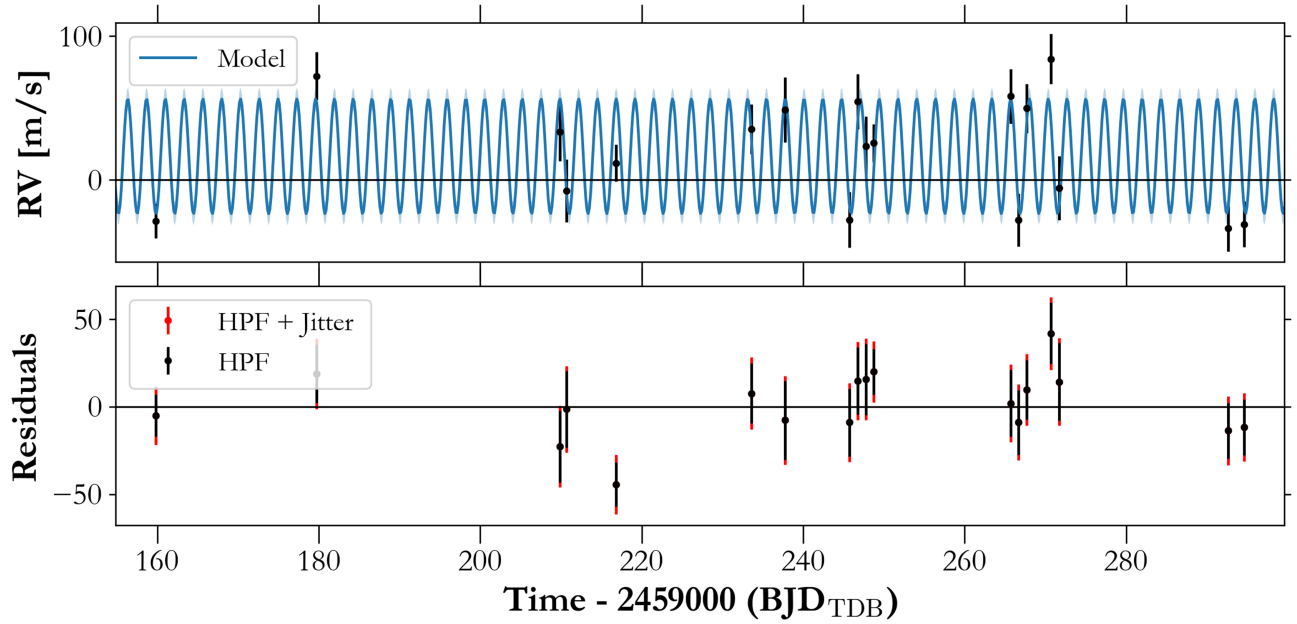

Figure 6. Time series of RV observations of TOI-532 with HPF. The best-fitting model derived from the joint fit to the photometry and RVs is plotted in blue, including the 16%–84% confidence interval in light blue. The bottom panel shows the residuals after subtracting the model. The jitter that is added in quadrature to the HPF error bars (is shown in red), and is negligible compared to the HPF error bars.

Table 2
HPF RVs of TOI-532

BJD_{TDB}	RV (m s^{-1})	σ (m s^{-1})
2459159.82217	−28.41	12.02
2459179.76468	72.25	16.71
2459209.85498	33.54	20.41
2459210.67441	−7.51	21.93
2459216.82807	11.79	12.70
2459233.61084	35.41	17.17
2459237.77469	48.57	22.57
2459245.75139	−27.58	19.35
2459246.74596	54.53	19.16
2459247.75757	23.59	20.39
2459248.74084	25.75	13.16
2459265.69221	58.13	19.00
2459266.69484	−27.78	18.47
2459267.68911	49.75	16.90
2459270.68444	84.04	17.46
2459271.68015	−5.66	22.22
2459292.62161	−33.47	15.94
2459294.61636	−30.69	15.83

the `SpEctrum Radial Velocity AnaLyser` pipeline (`SERVAL`; Zechmeister et al. 2018). `SERVAL` uses the template-matching technique to derive RVs (e.g., Anglada-Escudé & Butler 2012), where it creates a master template from the target star observations, and determines the Doppler shift for each individual observation by minimizing the χ^2 statistic. We create this master template by using all the HPF observations of TOI-532, where telluric and sky-emission lines are masked in the calculations of the RVs. The telluric regions identified by a synthetic telluric-line mask generated from `telfit` (Gullikson et al. 2014), a Python wrapper to the Line-by-Line Radiative Transfer Model package (Clough et al. 2005). Given the faintness of our target, we do not subtract out the sky fiber spectra from the sky fiber, as we observed that doing so added additional read noise, resulting in less precise RV measurements. To perform our barycentric correction, we use `barycorrpy`, the Python implementation (Kanodia & Wright 2018) of the algorithms from Wright & Eastman (2014). We obtained a total of 19 visits on this target between 2020 November 5 and 2021 March 21, of which one visit was discarded due to bad weather conditions. Each visit was divided into three exposures of 649 s each, where the median S/N of each HPF exposure was 37 per resolution element. The individual exposures were then binned after weighting, with the final binned RVs being listed in Table 2 and plotted in Figure 6.

3. Stellar Parameters

3.1. Spectroscopic Parameters with HPF-SpecMatch

Using the method described in Stefansson et al. (2020), we use the HPF spectra to estimate the $T_{\rm eff}$, $\log g$, and [Fe/H] values of the host star. This is based on `SpecMatch-Emp` algorithm from Yee et al. (2017), where we compare the high-resolution HPF spectra of TOI-532 to a library of high S/N as-observed HPF spectra, which consists of slowly rotating reference stars with well characterized stellar parameters from Yee et al. (2017).

We shift the observed target spectrum to a library wavelength scale and rank all of the targets in the library using a χ^2 goodness-of-fit metric. After this initial χ^2 minimization step, we pick the five best matching reference spectra (in this case: BD+29 2279, GJ 134, GJ 205, HD 28343, HD 88230) to construct a weighted spectrum using their linear combination to better match to the target spectrum (S. Jones et al. 2021, in preparation). In this step, each of the five stars receives a best-fit weight coefficient. We then assign the target stellar parameter $T_{\rm eff}$, $\log g$, and [Fe/H] values as the weighted average of the five best stars using the best-fit weight coefficients. Our final parameters are listed in Table 3, and are derived from the HPF order spanning 8670–8750 Å. As an

Table 3
Summary of Stellar Parameters for TOI-532

Parameter	Description	Value	Reference
Main identifiers:			
TOI	TESS Object of Interest	532	TESS mission
TIC	TESS Input Catalog	144700903	Stassun
2MASS	...	J05401918+1133463	2MASS
WISE	...	J054019.20+113345.6	WISE
Gaia EDR3	...	3340265717587057536	Gaia EDR3
Equatorial Coordinates, Proper Motion and Spectral Type:			
α_{J2016}	R.A. (R.A.)	85.08005702(4)	Gaia EDR3
δ_{J2016}	decl. (Decl.)	11.562632056(3)	Gaia EDR3
μ_α	Proper motion (R.A., mas yr^{-1})	23.24 ± 0.02	Gaia EDR3
μ_δ	Proper motion (Decl., mas yr^{-1})	-38.04 ± 0.01	Gaia EDR3
d	Distance in pc	134.61 ± 0.36	Bailer-Jones
$A_{V,max}$	Maximum visual extinction	0.01	Green
Optical and near-infrared magnitudes:			
B	Johnson B mag	15.769 ± 0.159	APASS
V	Johnson V mag	14.395 ± 0.056	APASS
g'	Sloan g' mag	15.136 ± 0.069	APASS
r'	Sloan r' mag	13.802 ± 0.065	APASS
i'	Sloan i' mag	13.068 ± 0.074	APASS
T	TESS magnitude	12.678 ± 0.007	Stassun
J	J mag	11.466 ± 0.023	2MASS
H	H mag	10.749 ± 0.024	2MASS
K_s	K_s mag	10.587 ± 0.025	2MASS
$W1$	WISE1 mag	10.488 ± 0.022	WISE
$W2$	WISE2 mag	10.541 ± 0.021	WISE
$W3$	WISE3 mag	10.436 ± 0.089	WISE
Spectroscopic Parameters[a]:			
$T_{\rm eff}$	Effective temperature in K	3957 ± 69	This work
[Fe/H]	Metallicity in dex	0.38 ± 0.04	This work
$\log(g)$	Surface gravity in cgs units	4.67 ± 0.12	This work
Model-Dependent Stellar SED and Isochrone fit Parameters[b]:			
$T_{\rm eff}$	Effective temperature in K	3927 ± 37	This work
[Fe/H]	Metallicity in dex	$0.338^{+0.072}_{-0.066}$	This work
$\log(g)$	Surface gravity in cgs units	$4.669^{+0.018}_{-0.017}$	This work
M_*	Mass in $M_\odot$	0.639 ± 0.023	This work
R_*	Radius in $R_\odot$	$0.612^{+0.013}_{-0.012}$	This work
L_*	Luminosity in $L_\odot$	$0.0803^{+0.0019}_{-0.0018}$	This work
ρ_*	Density in g cm^{-3}	$3.92^{+0.22}_{-0.21}$	This work
Age	Age in Gyrs	$7.1^{+4.4}_{-4.8}$	This work
Other Stellar Parameters:			
$v \sin i_*$	Rotational velocity in km s^{-1}	$<$2km s^{-1}	This work
ΔRV	"Absolute" radial velocity in km s^{-1}	9.67 ± 0.08	This work
U, V, W	Galactic velocities (Barycentric) in km s^{-1}	-2.22 ± 0.08, -30.20 ± 0.11, -1.24 ± 0.01	This work
U, V, W[c]	Galactic velocities (LSR) in km s^{-1}	8.89 ± 0.72, -17.96 ± 0.48, 6.01 ± 0.36	This work

Notes. References are: Stassun (Stassun et al. 2018), 2MASS (Cutri et al. 2003), Gaia EDR3 (Gaia Collaboration et al. 2021), Bailer-Jones (Bailer-Jones et al. 2018), Green (Green et al. 2019), APASS (Henden et al. 2018), WISE (Wright et al. 2010).
[a] Derived using the HPF spectral matching algorithm from Stefansson et al. (2020).
[b] EXOFASTv2 derived values using MIST isochrones with the Gaia parallax and spectroscopic parameters in *a*) as priors.
[c] The barycentric UVW velocities are converted into local standard of rest (LSR) velocities using the constants from Schönrich et al. (2010).

additional check, we performed a similar library comparison using six other HPF orders that have low telluric contamination, and obtain consistent stellar parameters across them. Our error estimates are obtained from using the cross-validation method, as described by Stefansson et al. (2020). During both optimization steps, we account for any potential $v \sin i$ broadening by artificially broadening the library spectra with a $v \sin i$ broadening kernel (Gray 1992) to match the rotational broadening of the target star. For TOI-532, we did not need significant rotational broadening, and therefore place an upper limit of $v \sin i < 2$ km s^{-1}, which is the lower limit of measurable $v \sin i$ values given HPF's spectral resolving power of $R \sim 55{,}000$.

3.2. Model-dependent Stellar Parameters

In addition to the spectroscopic stellar parameters derived above, we use EXOFASTv2 (Eastman et al. 2013) to model the spectral energy distribution (SED) of TOI-532 to derive model-dependent constraints on the stellar mass, radius, and age of the star. For the SED fit, EXOFASTV2 uses the BT-NextGen stellar atmospheric models (Allard et al. 2012). We assume Gaussian

priors on: (i) 2MASS *JHK* magnitudes; (ii) SDSS $g'r'i'$ and Johnson *B* and *V* magnitudes from APASS; (iii) *Wide-field Infrared Survey Explorer* magnitudes *W*1, *W*2, and *W*3 (Wright et al. 2010); (iv) spectroscopically derived host-star effective temperature, surface gravity, and metallicity; and (v) distance estimate from Bailer-Jones et al. (2021). We apply a uniform prior on the visual extinction and place an upper limit using estimates of Galactic dust by Green et al. (2019; Bayestar19) calculated at the distance determined by Bailer-Jones et al. (2021). We convert the Bayestar19 upper limit to a visual magnitude extinction using the $R_v = 3.1$ reddening law from Fitzpatrick (1999).

We use `GALPY` (Bovy 2015) to calculate the *UVW* velocities in the barycentric frame,[29] which along with the BANYAN tool (Gagné et al. 2018) classify TOI-532 as a field star in the thin disk with very high probability (Bensby et al. 2014).

3.3. Estimating Rotation Period

We note that the TESS photometry (PDCSAP undetrended photometry shown in Figure 1) is relatively flat, and shows no flaring activity. We also run a generalized Lomb Scargle periodogram (Zechmeister & Kürster 2009) on the TESS photometry using its `astropy` implementation, and find no significant peaks with a False Alarm Probability 1%.[30] This is consistent with an inactive star with a long rotation period.

4. Joint Fitting of Photometry and RVs

We perform a joint fit of all the photometry (TESS + ground-based sources), and the RVs using the `Python` packge `exoplanet`, which uses `PyMC3` the Hamiltonian Monte Carlo (HMC) package (Salvatier et al. 2016).

The `exoplanet` package uses `starry` (Luger et al. 2019) to model the planetary transits, using the analytical transit models from Mandel & Agol (2002), which includes a quadratic limb-darkening law. These limb-darkening priors are implemented in `exoplanet` using the reparameterization suggested by Kipping (2013) for uninformative sampling. We fit each phased transit shown in Figure 3 with separate limb-darkening coefficients.[31] In the photometric model we include a dilution factor for the TESS photometry, *D*, to represent the ratio of the out-of-transit flux of TOI-532 to that of all the stars within the TESS aperture, which has not been corrected for. We assume that the higher spatial resolution ground-based photometry has no dilution, since we use the ground-based transits to estimate the dilution in the TESS photometry. We assume the transit depth is identical in all bandpasses and use our ground-based transits to determine the dilution required in the TESS data to be $D_{\rm TESS} = 0.92 \pm 0.06$, which gives us a radius of 5.82 ± 0.19 $R_\oplus$. If the blending effects due to background stars are correctly accounted for by the SPOC pipeline, we expect this dilution term to be close to 1.

We model the RVs using a standard Keplerian model. We try an eccentric joint fit to the photometry and RVs, and obtain an eccentricity consistent with a circular orbit at $\sim 1\sigma$. Considering the Lucy–Sweeney bias (Lucy & Sweeney 1971), we adopt a circular orbit by fixing the eccentricity to 0, and the argument of periastron to 90°. For both the photometry and RV modeling, we include a simple white-noise model in the form of a jitter term that is added in quadrature to the error bars of each data set.

We use `scipy.optimize` to find the initial maximum a posteriori parameter estimates, which are then used as the initial conditions for parameter estimation using "No U-Turn Sampling" (Hoffman & Gelman 2014), implemented for the HMC sampler `PyMC3`, where we check for convergence using the Gelman–Rubin statistic ($\hat{R} \leqslant 1.1$; Ford 2006). We also run a joint fit using `juliet` (Espinoza et al. 2019), and verify that we obtain fit parameters similar to those from `exoplanet`.

The host stellar density constrained from the transit fit to the TESS photometry (Seager & Mallén-Ornelas 2003) is consistent with that obtained from the SED fit for an M0 host star (Section 3.2). The final derived planet parameters are shown in Table 4, and the phased HPF RVs are shown in Figure 7. We

Table 4
Derived Parameters for the TOI-532 System

Parameter	Units	Value
Orbital Parameters:		
Orbital Period	P (days)	2.3266508 ± 0.0000030
Eccentricity	e	0 (fixed)
Argument of Periastron	ω (degrees)	90 (fixed)
Semi-amplitude Velocity	K (m s^{-1})	$39.82^{+6.15}_{-5.98}$
Systemic Velocity[i]	γ (m s^{-1})	$16.42^{+5.04}_{-4.83}$
RV trend	dv/dt (m s^{-1} yr^{-1})	$0.35^{+5.08}_{-4.99}$
RV jitter	$\sigma_{\rm HPF}$ (m s^{-1})	$11.43^{+6.62}_{-8.84}$
Transit Parameters:		
Transit Midpoint	T_C (BJD$_{\rm TDB}$)	$2458470.576777^{+0.000860}_{-0.000902}$
Scaled Radius	R_p/R_*	0.0877 ± 0.0016
Scaled Semimajor Axis	a/R_*	$10.49^{+0.25}_{-0.23}$
Orbital Inclination	i (degrees)	$88.08^{+0.51}_{-0.41}$
Transit Duration	T_{14} (days)	0.0728 ± 0.001
Photometric Jitter[ii]	$\sigma_{\rm TESS}$ (ppm)	76^{+66}_{-45}
	$\sigma_{\rm RBO20201207}$ (ppm)	895^{+578}_{-584}
	$\sigma_{\rm TMMT20201215}$ (ppm)	434^{+482}_{-300}
	$\sigma_{\rm LCRO20210104}$ (ppm)	540^{+697}_{-382}
	$\sigma_{\rm TMMT20210104}$ (ppm)	823^{+789}_{-585}
	$\sigma_{\rm ARCTIC20210201}$ (ppm)	770^{+101}_{-98}
Dilution[iii]	$D_{\rm TESS}$	0.92 ± 0.06
Planetary Parameters:		
Mass	M_p ($M_\oplus$)	$61.5^{+9.7}_{-9.3}$
Radius	R_p ($R_\oplus$)	5.82 ± 0.19
Density	ρ_p (g cm^{-3})	1.72 ± 0.31
Semimajor Axis	a (au)	0.0296 ± 0.00035
Average Incident Flux[iv]	$\langle F \rangle$ (10^5 W m^{-2})	1.28 ± 0.11
Planetary Insolation	S ($S_\oplus$)	94.1 ± 8.0
Equilibrium Temperature[v]	$T_{\rm eq}$ (K)	867 ± 18

Notes.
[i] In addition to the Absolute RV from Table 3.
[ii] Jitter (per observation) added in quadrature to photometric instrument error.
[iii] Dilution due to presence of background stars in TESS aperture, not accounted for in the PDCSAP flux.
[iv] We use a Solar flux constant = 1360.8 W m^{-2}, to convert insolation to incident flux.
[v] We assume the planet to be a blackbody with zero albedo and perfect energy redistribution to estimate the equilibrium temperature.

[29] With *U* toward the Galactic center, *V* toward the direction of Galactic spin, and *W* toward the North Galactic Pole (Johnson & Soderblom 1987).
[30] The PDCSAP photometry from TESS flattens variability on timescales longer than about 10 days (Jenkins et al. 2016), and therefore our search using the TESS photometry is insensitive to stellar rotation periods longer than this.
[31] We also try fitting the photometry with a single set of limb-darkening coefficients for all the transits, and obtain similar results.

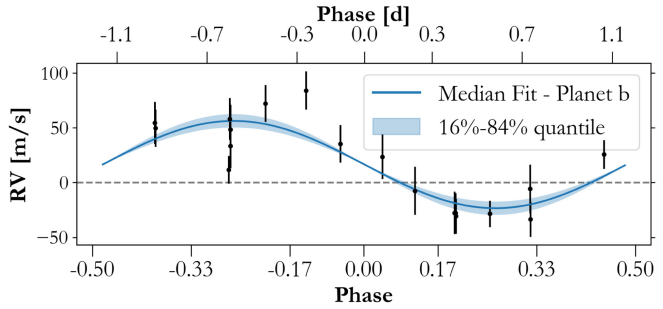

Figure 7. HPF RV observations phase folded on the best-fit orbital period from the joint fit from Section 4. The best-fitting model is shown in the solid line, whereas the 1σ confidence intervals are shown in blue.

obtain a mass for TOI-532b of $61.5^{+9.7}_{-9.3}$ $M_{\oplus}$, and a radius of 5.82 ± 0.19 $R_{\oplus}$.

5. Discussion

5.1. Giant Planet Dependence on Host-star Metallicity

In Figure 8(a) we show TOI-532 b with respect to other M-dwarf exoplanets with mass measurements at 3σ or higher. The data is taken from the NASA Exoplanet Archive (Akeson et al. 2013), and includes recent M-dwarf transiting planets discovered by TESS. TOI-532b has properties similar to three recent super Neptunes discovered by TESS that orbit M-dwarf stars—TOI-1728b (Kanodia et al. 2020), LP 714-417b (TOI-442 b; Dreizler et al. 2020), and TOI-674b (Murgas et al. 2021). TOI-532b represents the largest and most massive super Neptune found orbiting an M dwarf.

TOI-532b orbits a metal-rich M star, similar to the other gas giants found around M dwarfs (Figure 8(b)). This positive metallicity correlation favors the core-accretion formation mechanism (Pollack et al.1996; Schlaufman 2018); which can be explained if these gas giants formed due to the collisions of 10 $M_{\oplus}$ cores (Petigura et al. 2018). The probability of formation of these cores increases with metallicity, and therefore it should be easier to form such gaseous planet cores around metal-rich stars before the protoplanetary disk depletes (Ida & Lin 2004b). In situ formation of these gas giants at such orbital periods (and hence orbital separations) also requires super-Solar metallicity protoplanetary disks to provide enough material for the formation of their cores (Dawson et al. 2015; Boley et al. 2016; Batygin et al. 2016).

An alternative to the accretion theories of formation is gravitational instability (GI; Boss 1997). This has been proposed to explain the formation of gas giants around these low-mass stars (Boss 2006), especially the mid-to-late M dwarfs (Morales et al. 2019). The amount of material available in these disks would be too little to form cores that are massive enough to accrete gaseous envelopes from the disk before it gets depleted (Laughlin et al. 2004), lending credibility to GI as a potential formation mechanism. The discovery of gas giants such as TOI-532b, adds to the sparse population of these objects around M dwarfs, which can ultimately help differentiate between these two competing theories.

5.2. Neptune Desert

Figure 9 shows the Neptune desert which is characterized by a dearth of planets. We highlight the location of TOI-532b in the Neptune desert (Mazeh et al. 2016) in the Radius–Period plane (Figure 9(a)), where it falls in the middle of this region. The figure includes transiting exoplanets with mass measurements, colored according to their insolation, with the M-dwarf planets shown as solid markers, whereas those orbiting other spectral types hosts are translucent. Different processes have been proposed to explain this feature, which include photoevaporation (Ionov et al. 2018; Owen & Lai 2018), and high-eccentricity migration (Matsakos & Königl 2016).

Although typically parameterized in terms of orbital period, it is important to consider that in a combined sample of FGK and M-dwarf host stars, the bolometric insolation can differ by more than an order of magnitude for similar orbital separations (e.g., between a G-type host, and an early M dwarf). McDonald et al. (2019) suggest that this variation in the bolometric luminosity is the primary reason for the discrepancies in the location of the Neptune desert as a function of spectral type. Therefore, we also plot TOI-532 in the Radius–Insolation plane (Figure 9(b)), and include the desert boundaries from Mazeh et al. (2016), which were estimated using a predominantly FGK planet sample. We include these in the Insolation–Radius plane assuming a Solar mass and luminosity, and also assuming an M0 host star. While TOI-532 is located inside the Neptune desert in the Radius–Period plane, when accounting for the incident insolation, it is located by the edge of this desert. We therefore suggest that in order to compare a sample of planets across spectral types FGK, and M, the Neptune desert should be characterized in the Radius–Insolation plane.

The under density of planets in this highly irradiated region has often been attributed to atmospheric escape due to photoevaporation (Owen & Lai 2018). The rate and efficacy of photoevaporation is highly dependent on the X-ray and ultraviolet flux from the host star; where a planet around a midtype M dwarf can receive 100x more integrated X-ray flux than a solar type star (for the same insolation). When the frequency distribution of these gaseous planets is considered as a function of lifetime integrated X-ray flux, most of the variability between spectral types is accounted for (McDonald et al. 2019).

Characterization of planets such as TOI-532b, which lie within the Neptune desert, can help provide constraints on the potential formation mechanisms responsible for clearing out the Neptune desert. Estimating the fraction of H/He within its atmosphere would help bound the extent of photoevaporation, and its role in sculpting this desert. TOI-532b helps increase the small sample of planets situated inside this desert. Comparing the stellar (metallicity, age, stellar mass) and planetary parameters (density, planetary mass) for the sample of planets inside the desert to the larger exoplanet sample can help highlight potential formation mechanisms; perhaps as an extension to the radius valley (Fulton et al. 2017) and its dependence on various stellar properties (Owen & Murray-Clay 2018; Cloutier & Menou 2020; Berger et al. 2020; Van Eylen et al. 2021).

5.3. Planetary Composition and Photoevaporation

We use the giant planet models from Fortney et al. (2007) to estimate a core mass of ~36 $M_{\oplus}$ for TOI-532b, corresponding to an atmospheric mass (H/He) fraction of ~25%. Super Neptunes such as TOI-532b present an intermediate population of gaseous planets between sub-Neptunes (Bean et al. 2020) and Jovian planets (Mordasini et al. 2016; Dawson & Johnson 2018). A subset of these super Neptunes with equilibrium temperatures between 800–1200 K span the range where models predict a

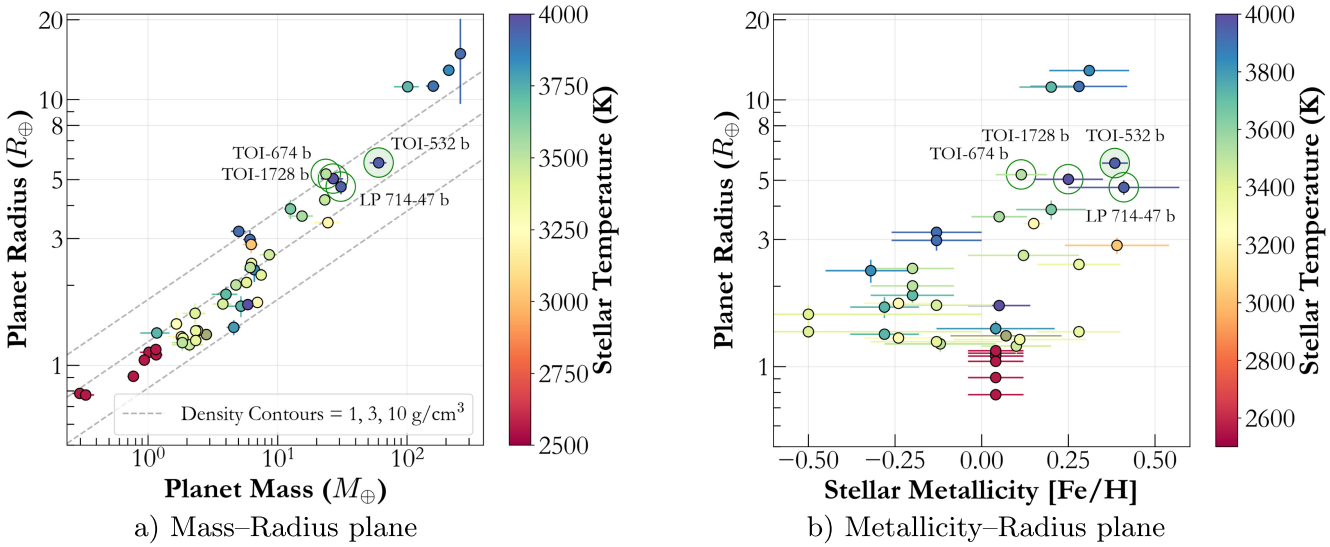

Figure 8. We show TOI-532b (circled) in different planet parameter space along with other M-dwarf planets with mass measurements at $>3\sigma$. (a) Mass–Radius plane for M-dwarf planets. We include contours of density 1, 3, 10 g cm^{-3}, where the markers are color coded by T_{eff}. (b) The metallicity of the host stars for the same planets. We note that all four super Neptunes highlighted in this plot are orbiting metal-rich early type M dwarfs.

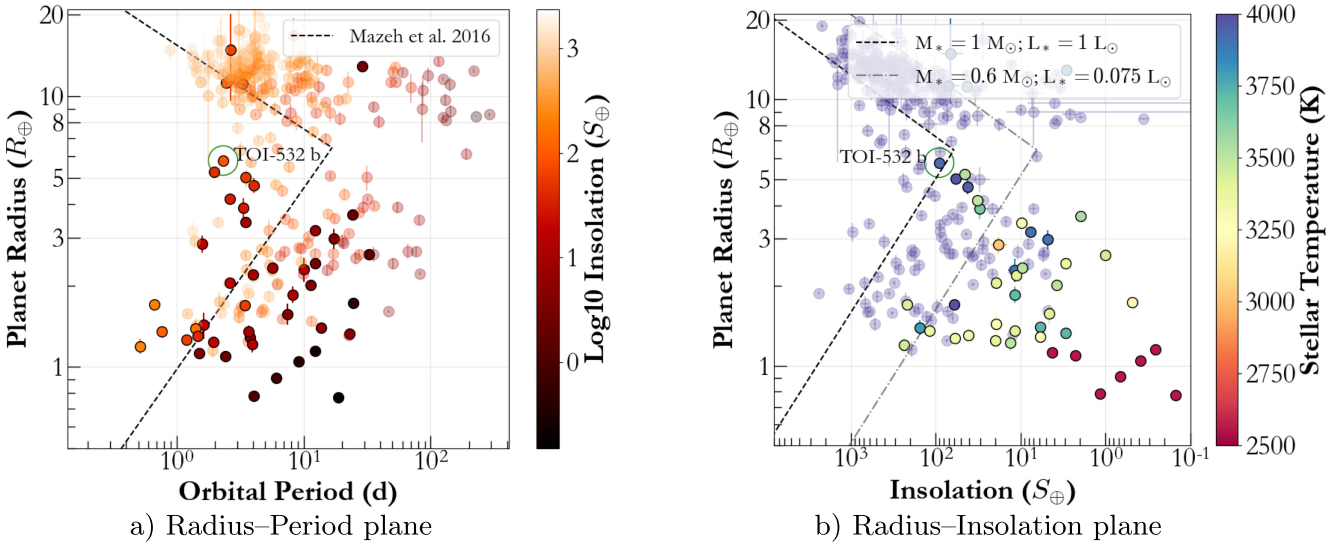

Figure 9. We note the location of TOI-532b in the Neptune desert (Szabó & Kiss 2011) along with a sample of transiting exoplanets that have their masses measured. (a) The sample in the Radius–Period plane is color coded by the log10 insolation, where the M-dwarf planets are solid whereas the rest are shown to be translucent. The nominal Neptune desert boundaries from Mazeh et al. (2016) are denoted with dashed lines. (b) We show TOI-532 in the Radius–Insolation plane, where M-dwarf planets are colored according to their T_{eff}, with planets orbiting other spectral type host stars denoted in purple. We use the Neptune Desert boundaries from Mazeh et al. (2016) in Radius–Period plane to calculate similar boundaries in the Insolation plane assuming 1 $M_\odot$ and 1 $L_\odot$ (Solar type star) in black, and with 0.6 $M_\odot$ and 0.075 $L_\odot$ (M0 star) in gray for representative purposes. Even though TOI-532 is placed in the middle of the Neptune desert in the Radius–Period plane, we note that in the Radius–Insolation plane it is placed by the edge of the desert, highlighting the importance of considering the insolation fluxes for planetary evolution.

transition from methane dominated atmospheres to carbon monoxide (Guzmán-Mesa et al. 2020). Characterizing the atmospheres of planets such as TOI-532b with equilibrium temperatures of ∼850 K by constraining their C/H and C/O ratios, can help place constraints on their formation history as well as atmospheric chemistry (Madhusudhan et al. 2017).

TOI-532 is relatively faint ($J = 11.46$), but is still accessible from 10-m class telescopes (Tamura et al. 2012; Kotani et al. 2018), as a potential target for detecting atmospheric escape using the He 10830 Å triplet. Considering the small number of suitable targets for such a measurement, we discuss the possibility of detecting atmospheric escape from TOI-532b. It is useful to compare TOI-532b to a similar planet with such a detection—GJ 3470b (Ninan et al. 2020; Palle et al. 2020)—and also to a planet without a He 10830 Å detection, TOI-1728b (Kanodia et al. 2020). In the energy limited mass outflow regime[32] the exosphere outflow is proportional to the irradiated extreme ultraviolet (EUV) flux and inversely proportional to the planet density. TOI-532 is an earlier M0 star than the M1.5 GJ 3470, with its spectral type more favorable with higher EUV radiation. However, TOI-532 is an older (and quieter) $7.2^{+4.6}_{-4.7}$ Gyr star, while GJ 3470 is relatively young at ∼3 Gyr.[33] If we consider the EUV flux from the host

[32] The energy limited regime is a reasonable assumption here since the gravitational potential of this planet is 12.81 erg g^{-1} (log10 (GM/R); Salz et al. 2016). This is not a system with a low-density upper atmosphere, like those seen in planets with higher gravitational potential (>13.3 erg g^{-1}).

[33] GJ 3470b stellar and planetary parameters are from Kosiarek et al. (2019).

star to be similar, due to the larger radius of the host star, the EUV irradiance on TOI-532b is 1.6 times that of GJ 3470b, which can make up for the 1.8 times higher density of TOI-532b than GJ 3470b. Thus, *if* the EUV flux of TOI-532 (7 Gyr, M0) is similar to GJ 3470 (3 Gyr, M1.5), we could expect a similar exosphere evaporation and mass outflow in TOI-532b like in GJ 3470b. Under this condition, He 10830 Å absorption during transit is a good probe to detect any signatures of outflow from TOI-532.

Conversely, the other planet TOI-1728b has a host star very similar to TOI-532 in both spectral type and age. TOI-532 orbits 1.25 times closer than TOI-1728b, and it is 1.5 times denser than TOI-1728b. Therefore, from a simple scaling relationship we expect the mass outflows in them to be only slightly less or very similar. That being said, TOI-1728b had a null detection of He 10830 Å with an upper limit of 1.1% (Kanodia et al. 2020). We therefore note that though the planetary parameters are amenable, the plausibility of a detectable outflow from this super Neptune hinges on the EUV irradiation environment of the host star.

6. Summary

In this work, we report the discovery and confirmation of a super Neptune, TOI-532b, orbiting an M0 star in a ∼2.3 day circular orbit. We detail the TESS photometry, ground-based follow-up photometry, high-contrast imaging, and also the RV observations performed using HPF. Furthermore, we discuss how the planet is situated at the edge of the Neptune desert in the Radius–Insolation plane, and discuss potential for He 10830 Å absorption detection using transmission spectroscopy. We also discuss the metallicity correlation for gas giants occurrence, and how it continues down to the M-dwarf spectral type.

The discovery and mass measurement of gas giants such as TOI-532b adds to the small sample of such planets around M-dwarf host stars, and can help inform theories of planetary formation and evolution. Therefore we encourage future observations to place limits on atmospheric escape using the He 10830 Å transition.

This research made use of Lightkurve, a Python package for Kepler and TESS data analysis (Lightkurve Collaboration 2018).

This paper is based on observations obtained from the Las Campanas Remote Observatory that is a partnership between Carnegie Observatories, the Astrophysics Corporation, Howard Hedlund, Michael Long, Dave Jurasevich, and SSC Observatories.

This work has made use of data from the European Space Agency (ESA) mission Gaia (https://www.cosmos.esa.int/gaia), processed by the Gaia Data Processing and Analysis Consortium (DPAC; https://www.cosmos.esa.int/web/gaia/dpac/consortium). Funding for the DPAC has been provided by national institutions, in particular the institutions participating in the Gaia Multilateral Agreement.

The Center for Exoplanets and Habitable Worlds is supported by the Pennsylvania State University, the Eberly College of Science, and the Pennsylvania Space Grant Consortium. These results are based on observations obtained with the Habitable-zone Planet Finder Spectrograph on the HET. We acknowledge support from NSF grants AST-1006676, AST-1126413, AST-1310885, AST-1517592, AST-1310875, AST-1910954, AST-1907622, AST-1909506, ATI 2009889, ATI-2009982, and the NASA Astrobiology Institute (NNA09DA76A) in the pursuit of precision radial velocities in the NIR. We acknowledge support from the Heising-Simons Foundation via grant 2017-0494. The Hobby–Eberly Telescope is a joint project of the University of Texas at Austin, the Pennsylvania State University, Ludwig-Maximilians-Universität München, and Georg-August Universität Gottingen. The HET is named in honor of its principal benefactors, William P. Hobby and Robert E. Eberly. The HET collaboration acknowledges the support and resources from the Texas Advanced Computing Center. We thank the Resident astronomers and Telescope Operators at the HET for the skillful execution of our observations of our observations with HPF.

We acknowledge support from NSF grants AST-1909506 and AST-1907622 and the Research Corporation for precision photometric observations with diffuser-assisted photometry.

This work was performed under the following financial assistance award 70NANB18H006 from U.S. Department of Commerce, National Institute of Standards and Technology.

This research has made use of the NASA Exoplanet Archive, which is operated by the California Institute of Technology, under contract with the National Aeronautics and Space Administration under the Exoplanet Exploration Program. This work includes data collected by the TESS mission, which are publicly available from MAST. Funding for the TESS mission is provided by the NASA Science Mission directorate. Some of the data presented in this paper were obtained from MAST. Support for MAST for non-HST data is provided by the NASA Office of Space Science via grant NNX09AF08G and by other grants and contracts.

This research has made use of the SIMBAD database, operated at CDS, Strasbourg, France, and NASA's Astrophysics Data System Bibliographic Services.

Some of the observations in this paper made use of the NN-EXPLORE Exoplanet and Stellar Speckle Imager (NESSI). NESSI was funded by the NASA Exoplanet Exploration Program and the NASA Ames Research Center. NESSI was built at the Ames Research Center by Steve B. Howell, Nic Scott, Elliott P. Horch, and Emmett Quigley.

Part of this research was carried out at the Jet Propulsion Laboratory, California Institute of Technology, under a contract with the National Aeronautics and Space Administration (NASA).

Computations for this research were performed on the Pennsylvania State University's Institute for Computational and Data Sciences Advanced CyberInfrastructure (ICDS-ACI), including the CyberLAMP cluster supported by NSF grant MRI-1626251. This is University of Texas Center for Planetary Systems Habitability contribution 0034. This work includes data from 2MASS, which is a joint project of the University of Massachusetts and IPAC at Caltech funded by NASA and the NSF. C.I.C. acknowledges support by NASA Headquarters under the NASA Earth and Space Science Fellowship Program through grant 80NSSC18K1114. S.K. would like to acknowledge Monae and Theodora for help with this project.

This research made use of exoplanet (Foreman-Mackey et al. 2021) and its dependencies (Kipping 2013; Robitaille et al. 2013; Theano Development Team 2016; Salvatier et al. 2016; Astropy Collaboration et al. 2018; Kumar et al. 2019; Luger et al. 2019; Agol et al. 2021; Foreman-Mackey et al. 2021). This research made use of Lightkurve, a Python package

for Kepler and TESS data analysis (Lightkurve Collaboration 2018).

Facilities: Gaia, HET (HPF), TESS, TMMT, LCRO, RBO, APO (ARCTIC), WIYN (NESSI), Shane (ShARCS), Exoplanet Archive.

Software: `ArviZ` (Kumar et al. 2019), AstroImageJ (Collins et al. 2017), `astroquery` (Ginsburg et al. 2019), `astropy` (Robitaille et al. 2013; Astropy Collaboration et al. 2018), `barycorrpy` (Kanodia & Wright 2018), `HxRGproc` (Ninan et al. 2018), `ipython` (Pérez & Granger 2007), `juliet` (Espinoza et al. 2019), `lightkurve` (Lightkurve Collaboration et al. 2018), `matplotlib` (Hunter 2007), `MRExo` (Kanodia et al. 2019), `numpy` (Oliphant 2006), `pandas` (McKinney 2010), `PyMC3` (Salvatier et al. 2016), `scipy` (Oliphant 2007; Virtanen et al. 2020), `SERVAL` (Zechmeister et al. 2018), `starry` (Luger et al. 2019; Agol et al. 2020), `Theano` (Theano Development Team 2016).

ORCID iDs

Shubham Kanodia https://orcid.org/0000-0001-8401-4300
Gudmundur Stefansson https://orcid.org/0000-0001-7409-5688
Caleb I. Cañas https://orcid.org/0000-0003-4835-0619
Marissa Maney https://orcid.org/0000-0001-8222-9586
Andrea S. J. Lin https://orcid.org/0000-0002-9082-6337
Joe P. Ninan https://orcid.org/0000-0001-8720-5612
Sinclaire Jones https://orcid.org/0000-0002-7227-2334
Andrew Monson https://orcid.org/0000-0002-0048-2586
Brock A. Parker https://orcid.org/0000-0001-9307-8170
Henry A. Kobulnicky https://orcid.org/0000-0002-4475-4176
Corey Beard https://orcid.org/0000-0001-7708-2364
Jack Lubin https://orcid.org/0000-0001-8342-7736
Paul Robertson https://orcid.org/0000-0003-0149-9678
Arvind F. Gupta https://orcid.org/0000-0002-5463-9980
Suvrath Mahadevan https://orcid.org/0000-0001-9596-7983
William D. Cochran https://orcid.org/0000-0001-9662-3496
Chad F. Bender https://orcid.org/0000-0003-4384-7220
Scott A. Diddams https://orcid.org/0000-0002-2144-0764
Connor Fredrick https://orcid.org/0000-0002-0560-1433
Samuel Halverson https://orcid.org/0000-0003-1312-9391
Suzanne Hawley https://orcid.org/0000-0002-6629-4182
Fred Hearty https://orcid.org/0000-0002-1664-3102
Leslie Hebb https://orcid.org/0000-0003-1263-8637
Ravi Kopparapu https://orcid.org/0000-0002-5893-2471
Andrew J. Metcalf https://orcid.org/0000-0001-5000-1018
Lawrence W. Ramsey https://orcid.org/0000-0002-4289-7958
Arpita Roy https://orcid.org/0000-0001-8127-5775
Christian Schwab https://orcid.org/0000-0002-0091-7105
Maria Schutte https://orcid.org/0000-0003-2435-130X
Ryan C. Terrien https://orcid.org/0000-0002-4788-8858
John Wisniewski https://orcid.org/0000-0001-9209-1808
Jason T. Wright https://orcid.org/0000-0001-6160-5888

References

Agol, E., Dorn, C., Grimm, S. L., et al. 2021, PSJ, 2, 38
Agol, E., Luger, R., & Foreman-Mackey, D. 2020, AJ, 159, 123
Akeson, R. L., Chen, X., Ciardi, D., et al. 2013, PASP, 125, 989
Allard, F., Homeier, D., & Freytag, B. 2012, RSPTA, 370, 2765
Anglada-Escudé, G., & Butler, R. P. 2012, ApJS, 200, 15
Astropy Collaboration, Price-Whelan, A. M., Sipőcz, B. M., et al. 2018, AJ, 156, 123
Bailer-Jones, C. A. L., Rybizki, J., Fouesneau, M., Demleitner, M., & Andrae, R. 2021, AJ, 161, 147
Bailer-Jones, C. A. L., Rybizki, J., Fouesneau, M., Mantelet, G., & Andrae, R. 2018, AJ, 156, 58
Bakos, G. A., Penev, K., Bayliss, D., et al. 2015, ApJ, 813, 111
Batygin, K., Bodenheimer, P. H., & Laughlin, G. P. 2016, ApJ, 829, 114
Bean, J. L., Raymond, S. N., & Owen, J. E. 2020, JGRE, 126, e06639
Bensby, T., Feltzing, S., & Oey, M. S. 2014, A&A, 562, A71
Berger, T. A., Huber, D., Gaidos, E., van Saders, J. L., & Weiss, L. M. 2020, AJ, 160, 108
Bessell, M. S. 1990, PASP, 102, 1181
Boley, A. C., Granados Contreras, A. P., & Gladman, B. 2016, ApJL, 817, L17
Boss, A. P. 1997, Sci, 276, 1836
Boss, A. P. 2006, ApJ, 643, 501
Bovy, J. 2015, ApJS, 216, 29
Burt, J. A., Nielsen, L. D., Quinn, S. N., et al. 2020, AJ, 160, 153
Cañas, C. I., Stefansson, G., Kanodia, S., et al. 2020, AJ, 160, 147
Clough, S. A., Shephard, M. W., Mlawer, E. J., et al. 2005, JQSRT, 91, 233
Cloutier, R., & Menou, K. 2020, AJ, 159, 211
Collins, K. A., Kielkopf, J. F., Stassun, K. G., & Hessman, F. V. 2017, AJ, 153, 77
Cutri, R. M., Skrutskie, M. F., van Dyk, S., et al. 2003, The IRSA 2MASS All-Sky Point Source Catalog (Pasadena, CA: NASA/IPAC)
Dawson, R. I., Chiang, E., & Lee, E. J. 2015, MNRAS, 453, 1471
Dawson, R. I., & Johnson, J. A. 2018, ARA&A, 56, 175
Dreizler, S. I. J., Crossfield, I. J. M., Kossakowski, D., et al. 2020, A&A, 644, A127
Dressing, C. D., & Charbonneau, D. 2015, ApJ, 807, 45
Eastman, J., Gaudi, B. S., & Agol, E. 2013, PASP, 125, 83
Espinoza, N., Bayliss, D., Hartman, J. D., et al. 2016, AJ, 152, 108
Espinoza, N., Kossakowski, D., & Brahm, R. 2019, MNRAS, 490, 2262
Fitzpatrick, E. L. 1999, PASP, 111, 63
Ford, E. B. 2006, ApJ, 642, 505
Foreman-Mackey, D., Luger, R., Agol, E., et al. 2021, JOSS, 6, 3285
Fortney, J. J., Dawson, R. I., & Komacek, T. D. 2021, JGRE, 126, e06629
Fortney, J. J., Marley, M. S., & Barnes, J. W. 2007, ApJ, 659, 1661
Fulton, B. J., Petigura, E. A., Howard, A. W., et al. 2017, AJ, 154, 109
Furlan, E., Ciardi, D. R., Everett, M. E., et al. 2017, AJ, 153, 71
Gagné, J., Mamajek, E. E., Malo, L., et al. 2018, ApJ, 856, 23
Gaia Collaboration, Brown, A. G. A., Vallenari, A., et al. 2021, A&A, 649, A1
Gaidos, E., Fischer, D. A., Mann, A. W., & Howard, A. W. 2013, ApJ, 771, 18
Ginsburg, A., Sipőcz, B. M., Brasseur, C. E., et al. 2019, AJ, 157, 98
Gray, D. F. 1992, Cambridge Astrophysics Series, Vol. 20 (Cambridge: Cambridge Univ. Press), 1
Green, G. M., Schlafly, E., Zucker, C., Speagle, J. S., & Finkbeiner, D. 2019, ApJ, 887, 93
Gullikson, K., Dodson-Robinson, S., & Kraus, A. 2014, AJ, 148, 53
Guzmán-Mesa, A., Kitzmann, D., Fisher, C., et al. 2020, AJ, 160, 15
Harrington, R. G. 1952, PASP, 64, 275
Henden, A. A., Levine, S., Terrell, D., et al. 2018, AAS Meeting, 232, 223.06
Hoffman, M. D., & Gelman, A. 2014, J. Mach. Learn. Res., 15, 1593
Hsu, D. C., Ford, E. B., & Terrien, R. 2020, MNRAS, 498, 2249
Huehnerhoff, J., Ketzeback, W., Bradley, A., et al. 2016, Proc. SPIE, 9908, 99085H
Hunter, J. D. 2007, CSE, 9, 90
Ida, S., & Lin, D. N. C. 2004a, ApJ, 604, 388
Ida, S., & Lin, D. N. C. 2004b, ApJ, 616, 567
Ionov, D. E., Pavlyuchenkov, Y. N., & Shematovich, V. I. 2018, MNRAS, 476, 5639
Jenkins, J. M., Twicken, J. D., McCauliff, S., et al. 2016, Proc. SPIE, 9913, 99133E
Johnson, D. R. H., & Soderblom, D. R. 1987, AJ, 93, 864
Johnson, J. A., Aller, K. M., Howard, A. W., & Crepp, J. R. 2010, PASP, 122, 905
Johnson, J. A., & Apps, K. 2009, ApJ, 699, 933
Kanodia, S., Cañas, C. I., Stefansson, G., et al. 2020, ApJ, 899, 29
Kanodia, S., Mahadevan, S., Ramsey, L. W., et al. 2018, Proc. SPIE, 10702, 107026Q
Kanodia, S., Wolfgang, A., Stefansson, G. K., Ning, B., & Mahadevan, S. 2019, ApJ, 882, 38
Kanodia, S., & Wright, J. 2018, RNAAS, 2, 4
Kasper, D. H., Ellis, T. G., Yeigh, R. R., et al. 2016, PASP, 128, 105005

Kipping, D. M. 2013, MNRAS, 435, 2152
Kopparapu, R. K., Hébrard, E., Belikov, R., et al. 2018, ApJ, 856, 122, publisher: American Astronomical Society
Kosiarek, M. R., Crossfield, I. J. M., Hardegree-Ullman, K. K., et al. 2019, AJ, 157, 97
Kotani, T., Tamura, M., Nishikawa, J., et al. 2018, Proc. SPIE, 10702, 1070211
Kumar, R., Carroll, C., Hartikainen, A., & Martin, O. A. 2019, JOSS, 4, 1143
Laughlin, G., Bodenheimer, P., & Adams, F. C. 2004, ApJL, 612, L73
Lightkurve Collaboration, Cardoso, J. V. D. M., Hedges, C., et al. 2018, Lightkurve: Kepler and TESS time series analysis in Python, Astrophysics Source Code Library, ascl:1812.013
Lucy, L. B., & Sweeney, M. A. 1971, AJ, 76, 544
Luger, R., Agol, E., Foreman-Mackey, D., et al. 2019, AJ, 157, 64
Madhusudhan, N., Bitsch, B., Johansen, A., & Eriksson, L. 2017, MNRAS, 469, 4102
Mahadevan, S., Ramsey, L., Bender, C., et al. 2012, Proc. SPIE, 8446, 84461S
Mahadevan, S., Ramsey, L. W., Terrien, R., et al. 2014, Proc. SPIE, 9147, 91471G
Maldonado, J., Micela, G., Baratella, M., et al. 2020, A&A, 644, A68
Mandel, K., & Agol, E. 2002, ApJL, 580, L171
Masci, F. J., Laher, R. R., Rusholme, B., et al. 2019, PASP, 131, 018003
Matsakos, T., & Königl, A. 2016, ApJL, 820, L8
Mazeh, T., Holczer, T., & Faigler, S. 2016, A&A, 589, A75
McDonald, G. D., Kreidberg, L., & Lopez, E. 2019, ApJ, 876, 22
McKinney, W. 2010, in Proc. of the 9th Python in Science Conf., ed. S. V. D. Walt & J. Millman, 56
Metcalf, A. J., Anderson, T., Bender, C. F., et al. 2019, Optic, 6, 233
Minkowski, R. L., & Abell, G. O. 1963, in Basic Astronomical Data: Stars and Stellar Systems, ed. K. A. Strand (Chicago, IL: Univ. Chicago Press), 481
Monson, A. J., Beaton, R. L., Scowcroft, V., et al. 2017, AJ, 153, 96
Morales, J. C., Mustill, A. J., Ribas, I., et al. 2019, Sci, 365, 1441
Mordasini, C., van Boekel, R., Mollière, P., Henning, T., & Benneke, B. 2016, ApJ, 832, 41
Murgas, F., Astudillo-Defru, N., Bonfils, X., et al. 2021, arXiv:2106.01246
Ninan, J. P., Bender, C. F., Mahadevan, S., et al. 2018, Proc. SPIE, 10709, 107092U
Ninan, J. P., Stefansson, G., Mahadevan, S., et al. 2020, ApJ, 894, 97
Oliphant, T. 2006, NumPy: A guide to NumPy (USA: Trelgol Publishing)
Oliphant, T. E. 2007, CSE, 9, 10
Owen, J. E., & Lai, D. 2018, MNRAS, 479, 5012
Owen, J. E., & Murray-Clay, R. 2018, MNRAS, 480, 2206
Palle, E., Nortmann, L., Casasayas-Barris, N., et al. 2020, A&A, 638, A61
Pérez, F., & Granger, B. E. 2007, CSE, 9, 21
Petigura, E. A., Marcy, G. W., Winn, J. N., et al. 2018, AJ, 155, 89
Pollack, J. B., Hubickyj, O., Bodenheimer, P., et al. 1996, Icar, 124, 62
Ricker, G. R., Winn, J. N., Vanderspek, R., et al. 2014, JATIS, 1, 014003
Robitaille, T. P., Tollerud, E. J., Greenfield, P., et al. 2013, A&A, 558, A33
Salvatier, J., Wiecki, T. V., & Fonnesbeck, C. 2016, PeerJ Comp. Sci., 2, e55
Salz, M., Schneider, P. C., Czesla, S., & Schmitt, J. H. M. M. 2016, A&A, 585, L2
Schönrich, R., Binney, J., & Dehnen, W. 2010, MNRAS, 403, 1829
Seager, S., & Mallén-Ornelas, G. 2003, ApJ, 585, 1038
Shetrone, M., Cornell, M. E., Fowler, J. R., et al. 2007, PASP, 119, 556
Srinath, S., McGurk, R., Rockosi, C., et al. 2014, Proc. SPIE, 9148, 91482Z
Stassun, K. G., Oelkers, R. J., Pepper, J., et al. 2018, AJ, 156, 102
Stefansson, G., Cañas, C., Wisniewski, J., et al. 2020, AJ, 159, 100
Stefansson, G., Hearty, F., Robertson, P., et al. 2016, ApJ, 833, 175
Stefansson, G., Mahadevan, S., Hebb, L., et al. 2017, ApJ, 848, 9
Szabó, G. M., & Kiss, L. L. 2011, ApJL, 727, L44
Tamura, M., Suto, H., Nishikawa, J., et al. 2012, Proc. SPIE, 8446, 84461T
Theano Development Team 2016, arXiv:abs/1605.02688
Tuomi, M., Jones, H. R. A., Butler, R. P., et al. 2019, arXiv:1906.04644
Van Eylen, V., Astudillo-Defru, N., Bonfils, X., et al. 2021, MNRAS, in press
Virtanen, P., Gommers, R., Oliphant, T. E., et al. 2020, NatMe, 17, 261
Wright, E. L., Eisenhardt, P. R. M., Mainzer, A. K., et al. 2010, AJ, 140, 1868
Wright, J. T., & Eastman, J. D. 2014, PASP, 126, 838
Yee, S. W., Petigura, E. A., & Braun, K. V. 2017, ApJ, 836, 77
Zechmeister, M., & Kürster, M. 2009, A&A, 496, 577
Zechmeister, M., Reiners, A., Amado, P. J., et al. 2018, A&A, 609, A12